

Computationally Efficient Implementation of Aperture Domain Model Image Reconstruction

Kazuyuki Dei¹, Siegfried Schlunk, *Student Member, IEEE*, and Brett Byram, *Member, IEEE*

Abstract—Aperture domain model image reconstruction (ADMIRE) is a useful tool to mitigate ultrasound imaging artifacts caused by acoustic clutter. However, its lengthy run-time impairs its usefulness. To overcome this drawback, we evaluated the reduced model methods with otherwise similar performance to ADMIRE. We also assessed other approaches to speed up ADMIRE, including the use of different levels of short-time Fourier transform (STFT) window overlap and examining the degrees of freedom of the model fit. In this study, we conducted an analysis of the reduced models, including those using Gram–Schmidt orthonormalization (GSO), singular value decomposition (SVD), and independent component analysis (ICA). We evaluated these reduced models using the data from simulations, experimental phantoms, and *in vivo* liver scans. We then tested ADMIRE’s performance using full, GSO, SVD, and ICA–fourth-order blind identification (ICA-FOBI) models. The results from simulations, experimental phantoms, and *in vivo* data indicate that a model reduced using the ICA-FOBI method is the most promising for accelerating ADMIRE implementation. In the *in vivo* liver data, the improvements in contrast relative to delay-and-sum (DAS) using a full model, GSO, SVD, and ICA-FOBI models are 6.29 ± 0.25 dB, 11.88 ± 0.90 dB, 9.01 ± 0.67 dB, and 6.36 ± 0.27 dB, respectively; whereas, the contrast-to-noise ratio (CNR) improvement values in the same order are 0.04 ± 0.06 dB, -1.70 ± 0.17 dB, -1.51 ± 0.19 dB, and 0.12 ± 0.07 dB, respectively. The implementation of ADMIRE using the reduced model methods can decrease ADMIRE’s computational complexity over three orders of magnitude. The use of a 50% STFT window overlap reduces ADMIRE’s serial run time by more than one order of magnitude without any remarkable loss of image quality, when compared to the use of a 90% window overlap used previously. Based on these findings, a combination of the ICA-FOBI model and the use of a 50% STFT window overlap makes the ADMIRE algorithm more computationally efficient.

Index Terms—Aperture domain signal, beamforming, dimensionality reduction, image quality, *in vivo*, medical ultrasound, physical model, reverberation clutter, signal processing, simulation.

I. INTRODUCTION

ULTRASOUND has been used extensively as a medical imaging modality, with an excellent safety record. It is also a real-time imaging method and is readily accessible and

affordable [1]. For these reasons, ultrasound imaging is one of the most frequently used tools for diagnosis and therapeutic guidance [2]–[4].

However, the imaging artifacts frequently encountered in clinical ultrasound are still problematic and impair its usefulness. These artifacts degrade ultrasound image quality, allowing a clinician to misinterpret an image, and obscure diagnosis [5]. The widely reported artifacts include: 1) beamwidth and off-axis artifacts caused by intrinsic characteristics of acoustic waves, decreasing spatial resolution, and contrast [6]; 2) attenuation artifacts producing acoustic enhancement and shadowing, related to the errors in attenuation of acoustic signals propagating through tissues [7]; 3) speed of sound artifacts, which are related to sound speed inhomogeneity in tissue, locally distorting wavefront of propagating and scattering waves (i.e., phase aberration) [8], [9], and also producing inconsistent images with actual appearance in the presence of gross sound speed errors [10]; and 4) reverberation artifacts, which occur when a transmitted signal is reflected back and forth between two interfaces during signal acquisition [11], which may severely degrade the images in modern ultrasound platforms [12]–[14].

To mitigate such artifacts, numerous beamformers have been developed [15]–[22], including a model-based beamformer called aperture domain model image reconstruction (ADMIRE) introduced by our group [14], [23]. Others have also recently applied these model-based methods to acoustics more generally [24], [25]. In the ADMIRE algorithm, we create a model based on the physics of wave propagation including multipath scattering. ADMIRE uses the model predictors to reconstruct decluttered images after decomposition and selection processes to identify scattering signals from the region of interest (ROI), as shown in Fig. 1. A reasonable analogy to ADMIRE would be electroencephalography (EEG) and magnetoencephalography (MEG) source localization methods [26], [27].

In our previous studies, we evaluated and demonstrated the algorithm’s performance and ability to mitigate ultrasound artifacts including off-axis, reverberation, and phase-aberration [23], [28]. ADMIRE is also robust to sound speed deviation, minimizing the speed of sound artifacts caused by gross sound speed mismatch [29]. ADMIRE can also be adapted to full field insonification sequences (i.e., plane wave imaging) to recover image quality in challenging high clutter environments with high levels of thermal noise [30]. Based on

Manuscript received December 2, 2018; accepted June 22, 2019. Date of publication June 26, 2019; date of current version September 25, 2019. This work was supported in part by NIH under Grant R01EB020040 and Grant S10OD016216-01 and in part by NSF under Grant 1750994. (Corresponding author: Kazuyuki Dei.)

The authors are with the Department of Biomedical Engineering, Vanderbilt University, Nashville, TN 37235 USA (e-mail: kazuyuki.dei@vanderbilt.edu). Digital Object Identifier 10.1109/TUFFC.2019.2924824

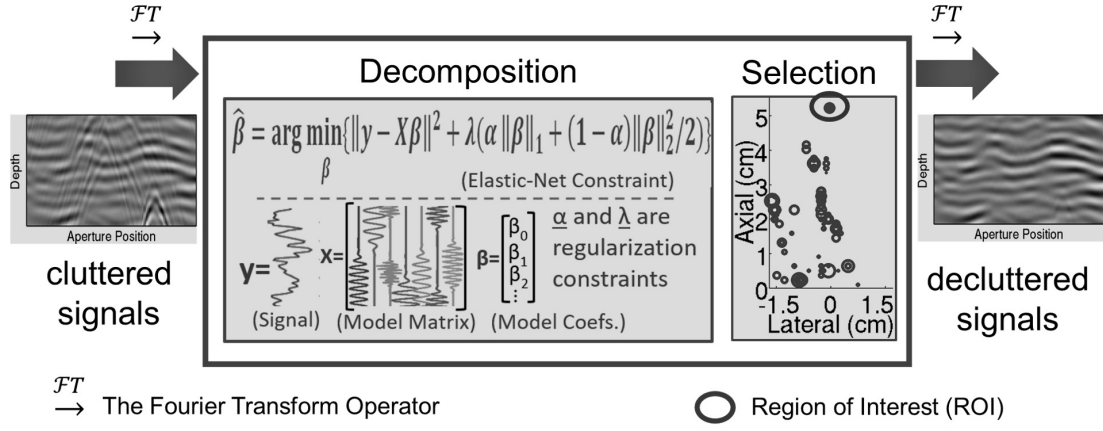


Fig. 1. Overview of ADMIRE algorithm. When implementing ADMIRE, the signal to the left is decomposed into wavefronts scattered from within the ROI and unwanted signals scattered from the clutter region. After decomposition, ADMIRE then reconstructs only signals from the ROI to form the signal on the right. Both decomposition and reconstruction processes are applied to the frequency domain data at each depth.

these findings, ADMIRE is a useful tool in reducing imaging artifacts in medical ultrasound.

However, a major problem with ADMIRE is its computational complexity, which impairs its usefulness. ADMIRE has high computational requirements caused by the large model and the nonlinear elastic-net regularization. The decomposition process must be repeated for every frequency per depth, further increasing the computational cost. We are interested in the reduced model methods and other strategies to reduce complexity without sacrificing improvements.

Previously, we examined the role of singular value decomposition (SVD) in reducing computational complexity [31]. It was computationally more efficient using orthonormal column vectors that are linearly independent, but its performance was reduced compared to ADMIRE. In this study, we aim to conduct a more comprehensive analysis to identify the usefulness of dimensionally reduced models when implementing ADMIRE. Here, we consider other models reduced using Gram–Schmidt orthonormalization (GSO) [32], [33] and independent component analysis (ICA) [34], in comparison with the images obtained using a full model or a model reduced using SVD. Furthermore, in considering other effects to accelerate ADMIRE, a simple solution may be to reduce the number of sliding window steps through depth. Similar to other beamforming methods [19], [35], [36], ADMIRE uses aperture domain signals in the frequency domain, incorporating a short-time Fourier transform (STFT) with a 90% window overlap. Based on these findings, we also evaluate the effects of different levels of STFT window overlap on image quality and run-time. In addition, we investigate the effect of the degrees of freedom selected during the model fit. Our ultimate goal is to enable an efficient and fast ADMIRE implementation while, otherwise, preserving its performance, thereby making ADMIRE more useful in real clinical applications.

II. METHODS

A. Overview of ADMIRE

Here, we summarize several important steps in the ADMIRE algorithm, while other details are available in [23]

and [28]–[30]. The ADMIRE model matrix X is constructed using model predictors, which is initially complex: $X \in \mathbb{C}^{\mathbb{M} \times \mathbb{N}}$, where \mathbb{M} is the number of aperture elements and \mathbb{N} is the total number of model predictors. The complex form of the ADMIRE model is converted into real (\Re) and imaginary (\Im) components and tiled as the following matrix form:

$$X = \begin{bmatrix} \Re\{p_{s_j}(x; t, \omega)\}^T & -\Im\{p_{s_j}(x; t, \omega)\}^T \\ \Im\{p_{s_j}(x; t, \omega)\}^T & \Re\{p_{s_j}(x; t, \omega)\}^T \end{bmatrix} \quad (1)$$

where j indexes model space sampling, p_{s_j} is the model predictor sampled at j th model space, x is the transducer aperture location, t and ω are the time and frequency to localize the signal, $X \in \mathbb{R}^{2\mathbb{M} \times 2\mathbb{N}}$. The model predictor can be formulated by the location (x_n, z_n) , where a signal is reflected from by delayed time τ_n , along with amplitude modulation term $A_n(x)$ across the transducer aperture [23], given by

$$p_{s_n}(x; t, \omega) = A_n(x) e^{j\omega\tau(x; x_n, z_n, \tau_n)}. \quad (2)$$

Using the model matrix in (1), the frequency domain data at a single frequency from each depth, denoted as $y \in \mathbb{R}^{2\mathbb{M} \times 1}$, in Fig. 1, can be expressed as a linear model, given by

$$y = X\beta \quad (3)$$

where β is the model coefficients for the real and imaginary components of the model predictors in X : $\beta \in \mathbb{R}^{2\mathbb{N} \times 1}$. Often, when implementing ADMIRE, the total number of model predictors is over a hundred times greater than the number of aperture elements (i.e., $\mathbb{M} < \mathbb{N}$), meaning that the solution of the linear model in (3) is a highly ill-posed inverse problem. To make the ill-posed problem stable, elastic-net regularization is used in model decomposition [37], as follows:

$$\hat{\beta} = \arg \min_{\beta} (\|y - X\beta\|^2 + \lambda(\alpha \|\beta\|_1 + (1-\alpha) \|\beta\|_2^2/2)) \quad (4)$$

where the first term represents the ordinary least squares, and the second term is the elastic-net regularization, combining the L1 norm with L2 norm, denoted as $\|\beta\|_1$ and $\|\beta\|_2$, respectively, using the tunable parameters of α and λ that determine the degree and type of regularization.

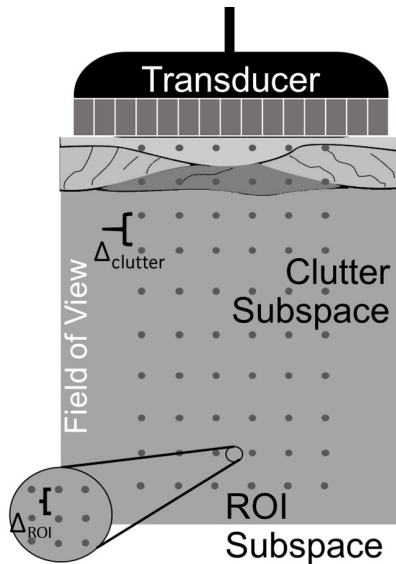


Fig. 2. ADMIRE model space is illustrated. The ADMIRE model space is sampled in two separated subspaces: 1) ROI subspace and 2) clutter subspace. Because it is also necessary to identify SOI using model predictors, the ADMIRE model space is finely sampled in the ROI subspace but not in the clutter subspace (i.e., $\Delta_{ROI} < \Delta_{clutter}$).

The last important step is to reconstruct the signals of interest (SOI) by selecting only model predictors and the corresponding coefficients within the region of interest (ROI), which is usually specified as an elliptical zone determined by the expected lateral and axial resolutions [23]

$$y_{ROI} = X_{ROI}\hat{\beta}_{ROI} \quad (5)$$

where y_{ROI} is the reconstructed signal of interest, which we also call the decluttered signal, X_{ROI} is the selected model predictors, and $\hat{\beta}_{ROI}$ is the corresponding coefficients. The decluttered signals in (5) are converted back into the original time domain using the inverse STFT (ISTFT) [38].

B. Model Space and Tunable Parameters

The ADMIRE model predictors in (2) are typically sampled from two subspaces, spatially divided into inside and outside ROI. We call the former ROI subspace, whereas the latter is referred to as clutter subspace, as demonstrated in Fig. 2. We rewrite the ADMIRE model matrix in (1), expressed as

$$X = [X_{ROI} \ X_{clutter}] \quad (6)$$

where X_{ROI} is the model predictors from the ROI subspace and $X_{clutter}$ is the predictors from the clutter subspace. We also note that the ADMIRE model space is finely sampled in the ROI subspace, but coarsely sampled in the clutter subspace (i.e., $\Delta_{ROI} < \Delta_{clutter}$). When reducing the ADMIRE model dimension, we apply a dimensionality reduction method separately to X_{ROI} and $X_{clutter}$ while preserving the unique aspect of each region. The reduced models from each subspace, having an $\mathbb{M} \times \mathbb{M}$ complex matrix, are combined, leading to $X_{reduced} \in \mathbb{C}^{\mathbb{M} \times 2\mathbb{M}}$. A complex form of the reduced model is

TABLE I
ADMIRE DEFAULT PARAMETERS

Parameter	Value
α	0.9
λ	$0.0189 \sqrt{y^T y}$
c_{lat}	6
c_{axl}	2
Model space (lateral) [m]	aperture length
Model space (axial) [m]	$\{0.001, z_r + (c_{axl}res_{axl})/2\}$
Model sampling [m]	
in ROI subspace	$\{0.0716res_{lat}, 0.286res_{axl}\}$
in clutter subspace	$\{1.43res_{lat}, 1.43res_{axl}\}$
STFT window size	$(8\log(2))/(2\pi BW f_c)$
STFT window overlap	90%

(x_r, z_r) is the center of the ROI specified in Fig. 2, c_{lat} and c_{axl} are lateral and axial scalable factors, res_{lat} and res_{axl} denote the lateral and axial resolutions [23], BW is the fractional bandwidth and f_c is the center frequency of transmitted pulse.

then decomposed into real (\Re) and imaginary (\Im) components and titled, the same as X in (1), where $X_{reduced} \in \mathbb{R}^{2\mathbb{M} \times 4\mathbb{M}}$.

It is also important to note that the ADMIRE algorithm and performance are primarily influenced by two factors. One is the model space sampling for each subspace as described above, and the other is the elastic-net regularization parameters, α and λ , in (4). Here, we focus only on the role of λ that controls the degrees of freedom (df) in this study because the dimensionality reduction will eliminate model space sampling as an important factor for run-time leaving λ as the most significant remaining factor [39]. We scaled a default value of λ set as $0.0189(y^T y)^{1/2}$. The default λ value and other ADMIRE parameters were determined in our previous findings [23], [28], [30], as indicated in Table I. Note that we implemented ADMIRE using a 90% STFT window overlap unless otherwise specified.

C. Computational Complexity

The total computational cost of the ADMIRE algorithm is high when compared to conventional delay-and-sum (DAS) beamforming. ADMIRE requires additional operations, including STFT, model decomposition, selection/reconstruction, and the ISTFT, which all increase its computational complexity. Table II summarizes the additional computational complexity of ADMIRE beyond that of DAS. When comparing each computational order, model fitting has a computational burden related to the number of predictors and predictors used, given by $\mathcal{O}(u^3 + u^2v)$, where u is the number of nonzero coefficients when fitting the data and v is the total number of model predictors in the matrix X in (1) [23], [30], [37]. Based on this, a reduced model could substantially decrease the computational time. Because the decomposition process must be repeated for every single frequency through depth, decreasing the total number of the

TABLE II
ADMIRE COMPUTATIONAL COMPLEXITY BEYOND DAS

Operation	Computational Cost
Short-time Fourier Transform (STFT)	$\mathcal{O}(pqr \log q)$
Model Decomposition	$\mathcal{O}(rw(u^3 + u^2v))$
Reconstruction	$\mathcal{O}(ru)$
Inverse short-time Fourier Transform (ISTFT)	$\mathcal{O}(r + qr \log q)$
Additional Computational Cost	$\mathcal{O}(r + rw(u^3 + u^2v) + ru + pqr \log q + qr \log q)$

p is the number of channels,

q is the number of samples per STFT window,

r is the total number of sliding window steps through depth determined by STFT window overlap,

u is the number of non-zero coefficients after fitting the data,

v is the total number of model predictors in the model matrix (changes per depth),

w is the number of frequencies used.

sliding window steps through depth (i.e., r) should also reduce complexity.

D. ADMIRE Using Dimensionality Reduced Models

We investigated several approaches for reducing the size of the model X in (1). Specifically, we examined the role of GSO [32], [33], SVD [40], [41], and ICA [34], [42]. In this section, we briefly look into each of these methods to understand how the transformed basis vectors construct a reduced model used for a computationally efficient ADMIRE implementation.

1) *Gram–Schmidt Orthogonalization*: Gram–Schmidt Orthogonalization (GSO), also called the Gram–Schmidt process, is a classic approach to constructing an orthonormal set from a given set of linearly dependent vectors [33]. The process starts with any one of the vectors in the set and sequentially forms the orthonormal vectors. Different outcomes are obtained from different orderings [32]. The dimension of a reduced model after applying GSO is $X_{\text{gso}} \in \mathbb{C}^{\mathbb{M} \times 2\mathbb{M}}$, much less than the original X (i.e., $2\mathbb{M} < \mathbb{N}$). We randomly reordered the model predictors in each subspace before applying GSO.

2) *Singular Value Decomposition*: Singular value decomposition (SVD) is widely used in matrix dimensionality reduction to make computations more efficient and decrease computational complexity. We use the SVD algorithm on subspaces of the ADMIRE model matrix in (6) to reduce the number of model predictors in each subspace. An SVD-based reduced model, denoted as X_{svd} , has the dimension reduced to $X_{\text{svd}} \in \mathbb{C}^{\mathbb{M} \times 2\mathbb{M}}$, the same as with X_{gso} .

3) *Independent Component Analysis*: Independent component analysis (ICA) removes higher order correlation [43], [44], leading to a set of separate independent sources that are statistically independent vectors. Given a linear mixture of underlying sources, we can reconstruct the underlying source with an unmixing matrix W . The aim of using ICA here is to solve the unmixing matrix and to form a reduced model using the columns of W^{-1} that are the independent components of the ADMIRE model, indicated by Shelens

[44]. The model reduced using ICA is statistically independent but not orthogonal and have a non-Gaussian distribution [34]. The model dimension after applying ICA is also by $X_{\text{ica}} \in \mathbb{C}^{\mathbb{M} \times 2\mathbb{M}}$ as with the other methods.

Because there is no analytical form to determine the unmixed matrix W , the ICA solution must involve estimation techniques [34]. These estimation algorithms are based on information theoretical principles, using maximum-likelihood, information maximization, marginal entropy, negentropy or non-Gaussianity maximization, and mutual information maximization, which are all related to one another [45]. In this study, we mostly used an ICA algorithm called the fourth-order blind identification (FOBI), which is probably the simplest method for performing ICA [44], [46]. In addition, we selected and compared four other ICA algorithms accounting for complex values scenarios: 1) RobustICA that is a deflated version of fastICA [42], [47] with complex data support [48], [49]; 2) complex ICA-EBM, representing complex ICA by entropy bound minimization (EBM) [50]–[52]; 3) second-order blind identification (SOBI) [53]; and 4) an algorithm for multiple unknown signals extraction (AMUSE) that may be useful in time structured signals or time series [54].

E. ADMIRE With Different Levels of STFT Window Overlap

When considering other effects to make ADMIRE more efficient and faster, we tested the impact of different levels of STFT window overlap on image quality using the simulated speckle-based target phantoms. We applied the STFT window overlap ratio, ranging from 0.05 to 0.95, when implementing ADMIRE using full and reduced models. We then assessed the resulting ADMIRE images qualitatively and quantitatively. In addition, we simulated a point target to compare point spread functions derived from DAS and full model ADMIRE implemented with a nonoverlap and 50% and 90% overlaps with the STFT window. We also quantified the full-width at half-maximum (FWHM) of the lateral beam profiles.

F. Simulated Phantom Data

We simulated speckle-based target phantoms with a 5-mm-diameter and 3-cm-deep anechoic cyst using Field II [55], [56].

TABLE III
FIELD II SIMULATION PARAMETERS

Parameter	Value
Number of elements	117
Number of mathematical elements (lateral)	15
Number of mathematical elements (elevational)	11
Height of element	4 mm
Width of element	0.254 mm
Kerf	0.003 mm
Lateral pitch	0.257 mm
Center frequency (f_c)	3 MHz
Sampling frequency: simulation ($f_{s, \text{sim}}$)	640 MHz
Sampling frequency: downsampled (f_s)	40 MHz
Fractional bandwidth	60%
Transmit focal depth	3 cm
Transmit/Receive f-number	1.0

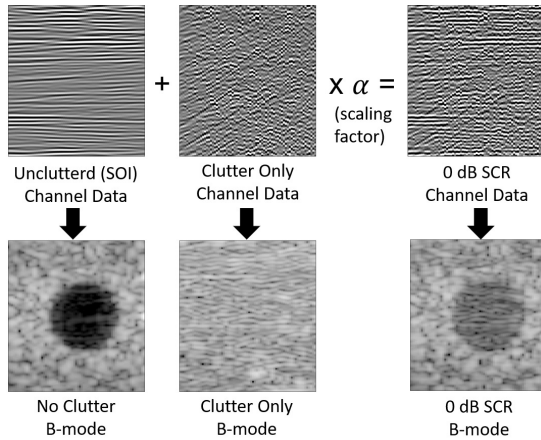


Fig. 3. Example to generate 0-dB SCR channel data by adding reverberation clutter to uncluttered (SOI) channel data. Top: Centered A-line channel data. Bottom: Corresponding simulated anechoic cyst B-mode images. The scaling factor, a , is computed by (7).

The background speckle was fully developed with 25 scatterers per resolution cell [57]. We generated six speckle realizations. A linear array transducer was modeled with 3.0-MHz center frequency and 60% fractional bandwidth with transmit focal depth of 3 cm, as summarized in Table III. We also added various levels of reverberation clutter relative to SOI, given by signal-to-clutter ratio (SCR)

$$\text{SCR} = 10 \log_{10} \left(\frac{\text{Power}_{\text{SOI}}}{\text{Power}_{\text{Clutter}}} \right). \quad (7)$$

We simulated -20 -, -10 -, 0 -, 10 -, and 20 -dB SCRs using an efficient pseudo nonlinear simulation tool [58], [59]. The tool allows for the fast simulation of realistic reverberation clutter, providing a paired channel data set for SOI and clutter. We then apply a scaling factor, computed by (7) to cluttered channel data for each SCR case. The scaled cluttered data are summed with the corresponding SOI channel data. The process is repeatedly applied to each A-line channel data. Fig. 3 shows an example to generate 0-dB SCR simulated data.

We evaluated the resulting images formed after ADMIRE using full and reduced models. We applied the default value

TABLE IV
C5-2 CURVILINEAR TRANSDUCER AND
VERASONICS SYSTEM SETTINGS

Parameter	Value
Sector	75°
Number of elements	128
Pitch	0.425 mm
Center frequency (f_c)	3.125 MHz
Sampling frequency (f_s)	12.5 MHz
Fractional bandwidth	60%
Transmit focal depth	3 cm
Transmitted pulse	1.5 cycles
Transmit/Receive f-number	1.0
Speed of sound (c)	1540 m/s

of λ scaled by $1/2$, (i.e., $0.0189\sqrt{y^T y}/2$). We tested the usefulness of reduced models using the methods in comparison with images formed using a full model. We also added DAS images in order to quantify relative improvements of ADMIRE images from DAS beamforming.

G. Experimental Phantom Data

We also applied ADMIRE using these reduced models to the experimental phantom data to test whether the simulation results correlate with experimental findings. We acquired data from a tissue-mimicking phantom (Multi-Purpose Multi-Tissue Ultrasound Phantom 040GSE, CIRS Inc., Norfolk, VA, USA) using a Verasonics Vantage Ultrasound System (Verasonics, Inc., Kirkland, WA, USA). We used a C5-2 curvilinear array transducer to acquire 128 A-lines over a 75° sector, which is the same probe setting we used for our previous study [29]. Table IV summarizes the settings for the curvilinear probe and the Verasonics ultrasound system.

The experimental data were beamformed using DAS, ADMIRE using a full model and three reduced models based on: 1) GSO; 2) SVD; and 3) ICA-FOBI methods. In addition, with the experimental data, we compared five ICA algorithms using image quality metrics and speckle statistics. We applied the default value of λ scaled by $1/2$ in the implementation of ADMIRE.

H. In Vivo Data

We acquired *in vivo* abdominal and liver data from a healthy human subject using the same Verasonics ultrasound system and the same C5-2 transducer. The acquisition sequences and parameter settings are also indicated in Table IV. We applied ADMIRE to the *in vivo* data using the same models tested in the experimental data. We also applied five different λ parameters, scaled by factors of $1/10$, $1/5$, $1/2$, 1 , and 2 , to the default λ value to test how the parameters of λ (i.e., the degrees of freedom df) impact ADMIRE's performance and efficiency using a reduced model. The Vanderbilt University Institutional Review Board approved the study.

I. Image Quality Metrics and Speckle Statistics

We compared the outcomes using contrast (C), contrast-to-noise ratio (CNR), and speckle signal-to-noise ratio (SSNR) of

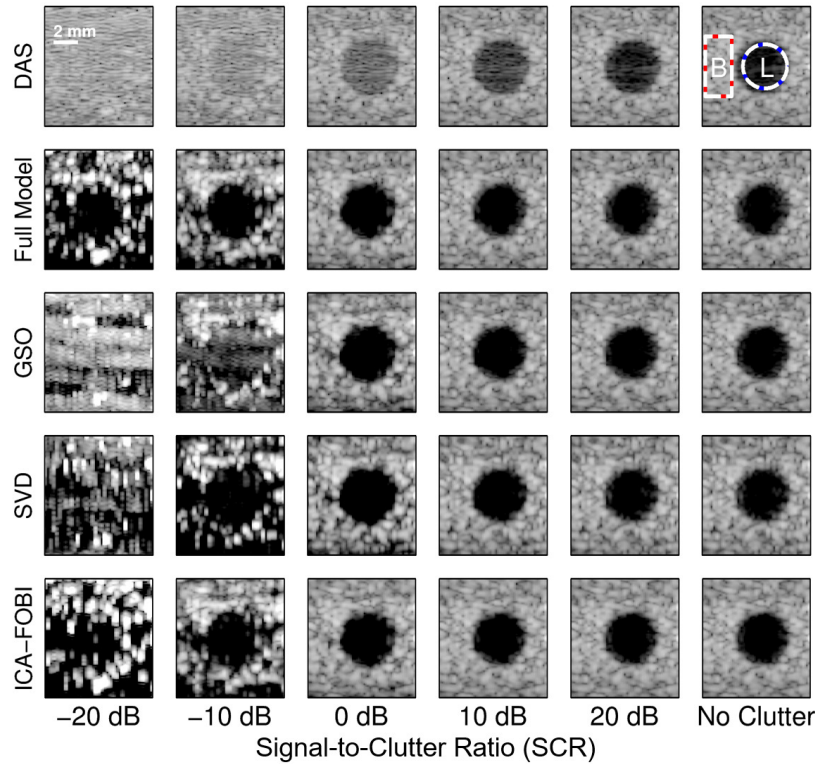


Fig. 4. B-mode images of simulated anechoic cyst phantom reconstructed after applying DAS, ADMIRE using a full model and three reduced models based on the GSO, SVD, and ICA-FOBI methods. The phantom has 5-mm-diameter 3-cm-deep anechoic cyst simulated using Field II. Reverberation clutter ranging from -20 - to 20 -dB SCRs was also added using our pseudo nonlinear simulator [58]. DAS B-mode image in the top left indicates two regions used for image quality metrics and speckle statistics measurements. We denote lesion and background, corresponding to inside and outside an anechoic structure, as L or B, respectively. The dynamic range is 60 dB.

B-mode data acquired from simulations, experimental tissue-mimicking phantoms, and *in vivo* scans

$$C = -20 \log_{10} \left(\frac{\mu_l}{\mu_b} \right) \quad (8)$$

$$\text{CNR} = 20 \log_{10} \left(\frac{|\mu_l - \mu_b|}{\sqrt{\sigma_l^2 + \sigma_b^2}} \right) \quad (9)$$

$$\text{SSNR} = \frac{\mu_b}{\sigma_b} \quad (10)$$

where (μ_l, σ_l^2) and (μ_b, σ_b^2) are the value of (mean, variance) of the uncompressed enveloped data inside and outside anechoic or hypoechoic structures, respectively.

J. Timing Measurements

We evaluated timing reduction using simulated phantoms and *in vivo* liver data. We measured the total single-core serial run time for each case of ADMIRE in MATLAB (The Mathworks Inc., Natick, MA, USA) on a 3.40-GHz CPU desktop computer. Timing measurements were conducted in several scenarios, including ADMIRE using various λ values and with different levels of STFT window overlap ratio. We were also interested in computing the computational order from the total number of model predictors and the number of nonzero coefficients using full and reduced models through depth.

III. RESULTS

A. Reduced Model Evaluation Using Simulations

Fig. 4 shows the B-mode images of a simulated anechoic cyst phantom reconstructed after applying ADMIRE using a full model and three reduced models based on the GSO, SVD, and ICA-FOBI methods, along with conventional DAS beamforming. When comparing the resulting ADMIRE images qualitatively, there are no noticeable differences in moderate or lower clutter environments. However, there are substantial discrepancies in image quality between each model in high clutter scenarios (i.e., the range of $\text{SCR} \leq -10$ dB). They all have image artifacts at -20 -dB SCR. The images obtained from ADMIRE using the GSO-based reduced model also include very obvious image artifacts in the presence of clutter of -10 -dB SCR. It is also interesting to note that the ICA-FOBI reduced model may provide improved performance of ADMIRE, compared to the other two reduced models, throughout the range of clutter levels.

The matched quantitative results are presented using a box plot shown in Fig. 5. For both contrast and CNR values, we measured relative improvements of post-ADMIRE images to DAS B-mode images, but SSNR values were compared to the ideal value of 1.91 [57]. Unsurprisingly, ADMIRE improves contrast and CNR in moderate clutter environments while preserving speckle statistics in the cases of ADMIRE

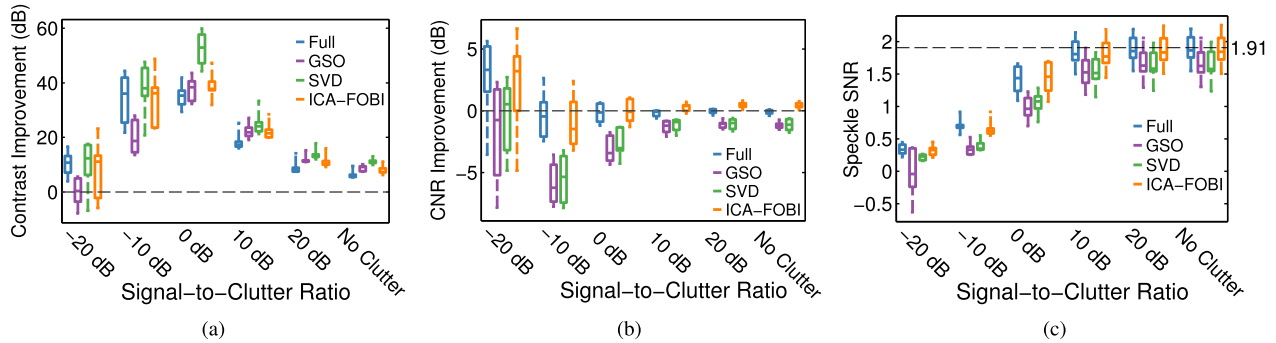


Fig. 5. Box plots of the matched quantitative results of the B-mode images shown in Fig. 4, including (a) contrast (ΔC) and (b) CNR (ΔCNR) improvements relative to DAS, along with (c) SSNR. There are six speckle realizations. These results show good correlation with qualitative indications, as demonstrated in Fig. 4.

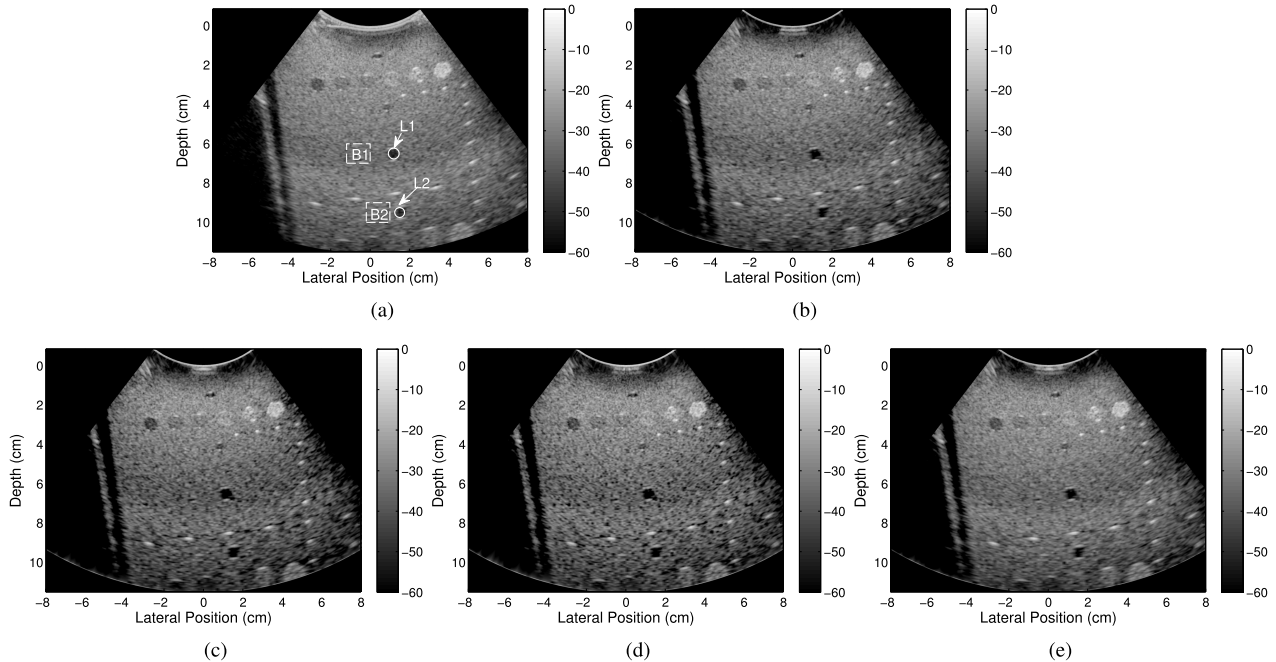


Fig. 6. B-mode images reconstructed using experimentally acquired data on a tissue-mimicking phantom. The images were formed after applying DAS and ADMIRE using different models when implemented, including a full model and three reduced models using the GSO, SVD, and ICA-FOBI methods. The dynamic range is 60 dB. The DAS B-mode image also indicates two sets of regions used to compute contrast, CNR, and SSNR. The measured contrast, CNR, and SSNR values were averaged with the standard deviation. The corresponding results are summarized in Table V. (a) DAS. (b) Full model. (c) GSO model. (d) SVD model. (e) ICA-FOBI model.

using full or ICA-based model. These findings are consistent with the results reported in our previous study [30].

In comparison with the performance of ADMIRE using three reduced models, the qualitative and quantitative results are consistent, indicating that ADMIRE performance using the ICA-FOBI reduced model is the most similar to that of using a full model. It is worth noting that ADMIRE using an SVD-based reduced model provides higher contrast while decreasing the value of CNR and SSNR. These SVD findings have been reported in our previous study [31], which may produce dark region artifacts [60] and decrease the dynamic range [61].

B. Reduced Model Evaluation Using Tissue-Mimicking Phantom

Fig. 6 demonstrates the methods on the experimental phantom data. The figure also includes the matched DAS B-mode

image, indicating two sets of regions used to calculate image quality metrics and SSNR. We then averaged the measured image metrics, along with the standard deviation. The matched contrast, CNR, and SSNR values are summarized in Table V. These results from experimental tissue-mimicking phantom data are mostly consistent with the results reported in the simulations, suggesting that the ICA-FOBI reduced model allows ADMIRE to perform as well as ADMIRE performance using a full model.

C. Reduced Model Evaluation Using In Vivo Liver Scan Data

Fig. 7 evaluates the results of using the reduced models with *in vivo* abdominal liver scan data. Fig. 7(a) demonstrates four sets of ADMIRE images reconstructed from implementing ADMIRE with different models, with various values of the tunable parameter λ (the default value set as $0.0189\sqrt{y^T y}$).

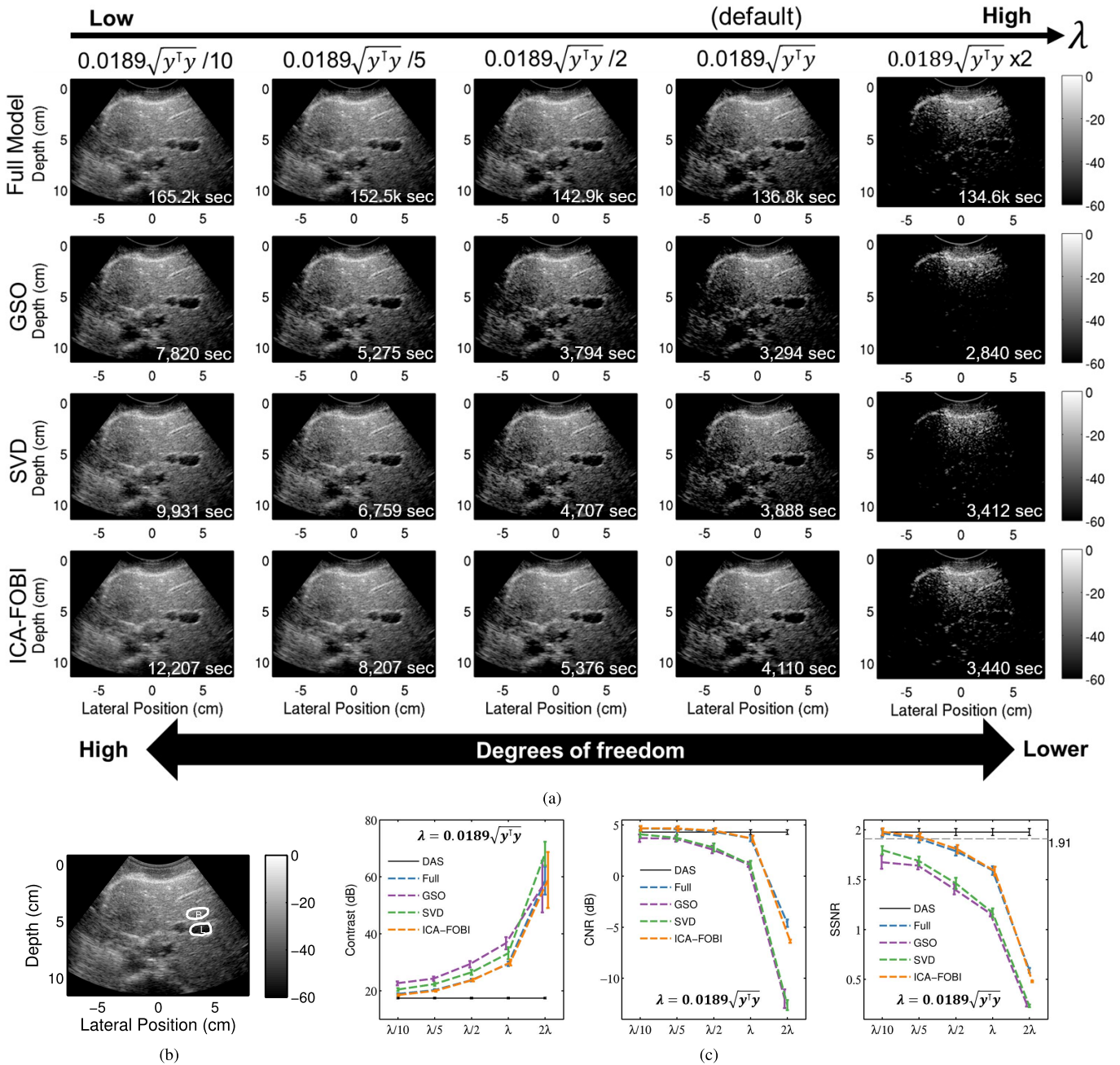


Fig. 7. *In vivo* abdominal and liver B-mode images formed from the data acquired using a Verasonics Vantage Ultrasound System with a C5-2 curvilinear array transducer. ADMIRE B-mode images were obtained from ADMIRE using a combination of different models and tunable parameter λ , in order to examine how the ADMIRE performance relates to the model and the degrees of freedom that are controlled by the parameter of λ . The top in (a) shows the resulting images using ADMIRE with a full model as a function of λ . The rest in (a) is the ADMIRE images using a model reduced using the GSO, SVD, and ICA-FOBI methods. Each demonstrated image indicates the total single-core serial run time to reconstruct in the lower right corner. We also include the matched DAS B-mode image in (b), indicating two regions, L (lesion or hypoechoic structure) and B (background), used to measure image quality metrics and speckle statistics. The dynamic range is 60 dB. The matched quantitative results of contrast, CNR, and SSNR as a function of λ are reported in (c). (a) ADMIRE B-mode images as a function of λ or degrees of freedom (*df*). (b) DAS B-mode with mask regions. (c) Contrast, CNR, and SSNR as a function of λ .

The timing is included in the figure. Fig. 7(b) shows the matched DAS B-mode image, and Fig. 7(c) reports the matched quantitative results of contrast, CNR, and SSNR as a function of λ . The metrics were calculated using the mask regions, L and B, indicating inside and outside anechoic or hypoechoic tissue structures, respectively, in Fig. 7(b). Note that ADMIRE using an ICA-FOBI reduced model performs

as well as the use of a full model as a function of λ . The finding suggests that the ICA-FOBI reduced model has no significant impact when varying the value of λ . It is also noted that ADMIRE using the GSO- or an SVD-based reduced model may increase the performance if λ is adaptively tuned to match the use of full model ADMIRE, which usually requires higher degrees of freedom, as demonstrated in Fig. 7(c).

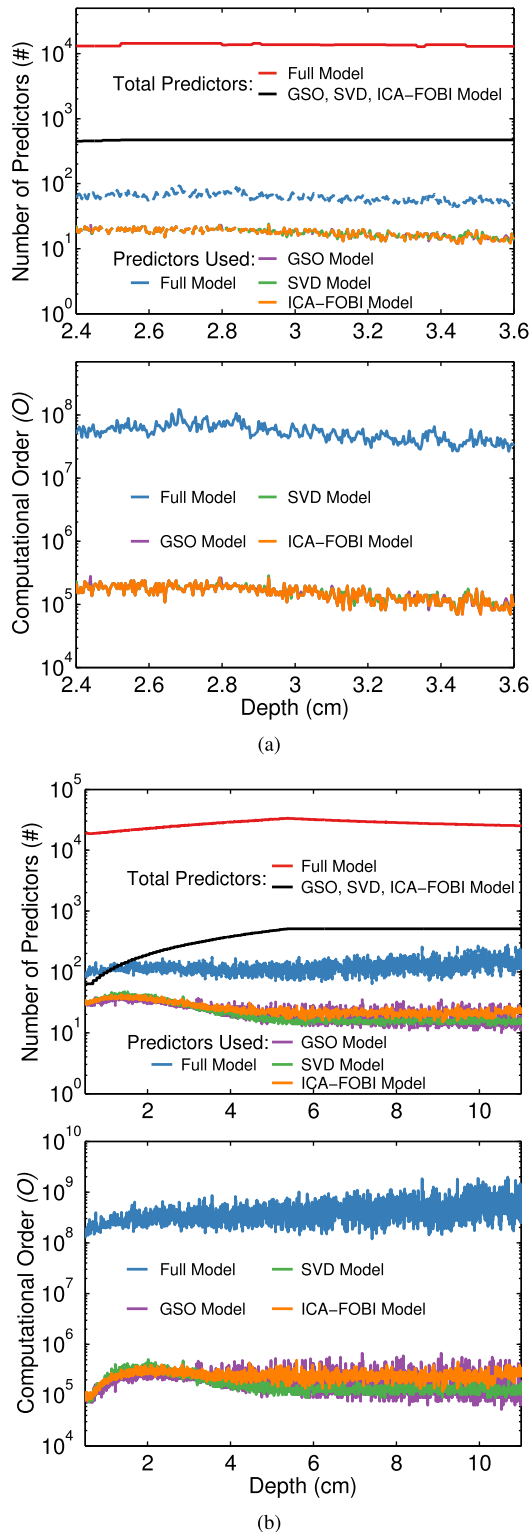


Fig. 8. Top figures report the total number of predictors and the number of predictors used (i.e., the number of nonzero coefficients) per depth while implementing ADMIRE using full and reduced models to (a) simulated phantom and (b) *in vivo* liver scan data. The corresponding computational order in model decomposition is also demonstrated.

D. Reduced Model Dimension and Computational Cost Reduction

We identified the total number of predictors and the number of predictors used while implementing ADMIRE using full and reduced models. Fig. 8 indicates the significant

TABLE V
TISSUE-MIMICKING PHANTOM IMAGE QUALITY METRICS
AND SPECKLE STATISTICS (SIX REALIZATIONS)

	Contrast (dB)	CNR (dB)	SSNR
DAS	8.78 ± 0.49	1.11 ± 0.53	2.23 ± 0.17
Full	11.47 ± 0.15	1.23 ± 0.20	2.02 ± 0.27
GSO	13.65 ± 0.13	0.55 ± 0.59	1.72 ± 0.23
SVD	13.43 ± 0.26	0.36 ± 0.61	1.58 ± 0.20
ICA-FOBI	11.66 ± 0.35	1.38 ± 0.25	2.12 ± 0.26

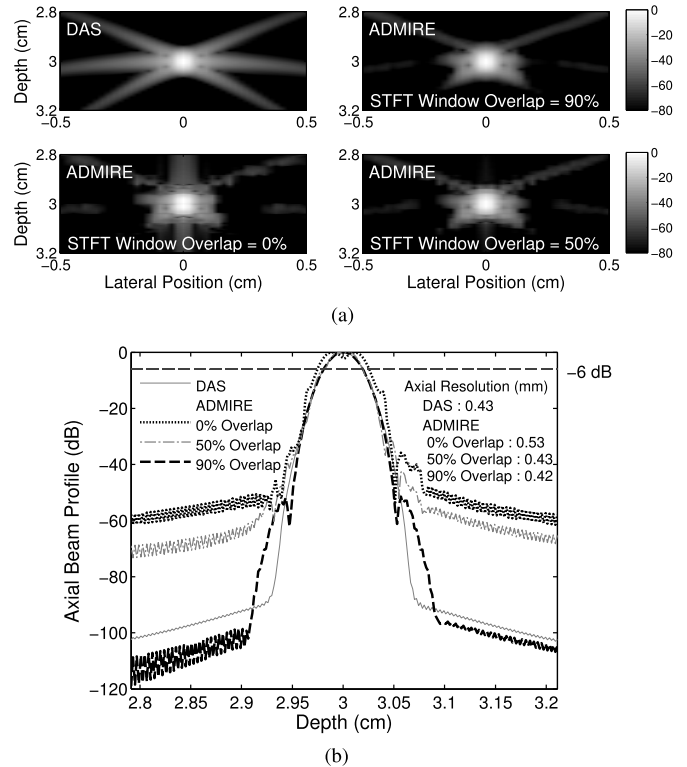


Fig. 9. 2-D PSFs simulated using DAS and full model ADMIRE with different levels of STFT window overlap ratio are shown in (a). The corresponding axial beam profiles in (b) are used to quantify the axial spatial resolution, also indicated in (b). The dynamic range of 2-D PSF images is 80 dB.

dimensionality reduction in the reduced models from simulated phantom and *in vivo* liver data, indicating that computational complexity is reduced by three orders of magnitude compared to the computational cost of applying a full-sized model.

E. Impact on Image Quality With Different Levels of STFT Window Overlap

Fig. 9 shows the set of 2-D point spread functions (PSFs) derived from DAS and ADMIRE, using different levels of STFT window overlap, together with the corresponding axial beam profiles. We also quantified the spatial resolution axially, as indicated at top right in Fig. 9(b). It is worth noting that ADMIRE using a 50% STFT window overlap provides axial resolution as high as that derived from DAS. However, the off-peak lobes persist at a much higher level when compared to the case of ADMIRE using a 90% window overlap.

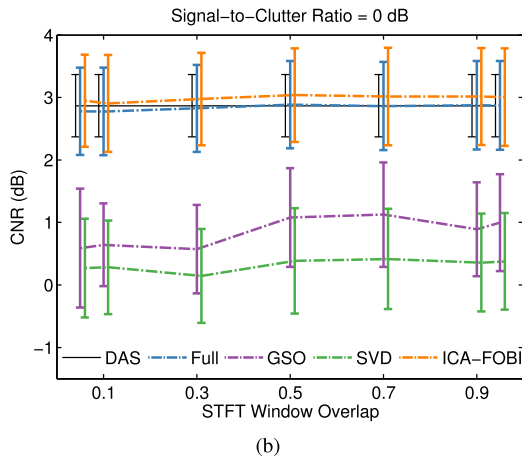
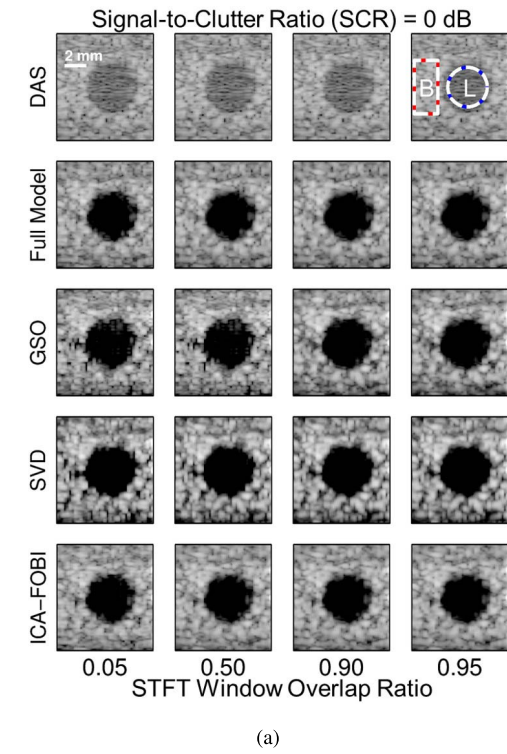


Fig. 10. Simulated anechoic cyst images formed after DAS and ADMIRE using four different models with different levels of STFT window overlap, ranging from 0.05 (5%) to 0.95 (95%) are demonstrated in (a). The images are reconstructed after adding reverberation clutter at SCR 0 dB. The dynamic range is 60 dB. (b) Matched CNR as a function of an STFT window overlap ratio.

Apart from a point target simulation to demonstrate resolution impact, we used simulated cyst phantoms with reverberation clutter at SCR 0 dB to examine how ADMIRE image quality may be correlated with the ratio of STFT window overlap. Fig. 10(a) demonstrates the qualitative results obtained from DAS and ADMIRE, using four different models with different levels of STFT window overlap, ranging from 0.05 to 0.95, while the matched CNR values are reported using line plots with error bars in Fig. 10(b). The results demonstrate that ADMIRE images reconstructed using STFT window overlap lower than 50% may be degraded to some extent, but the

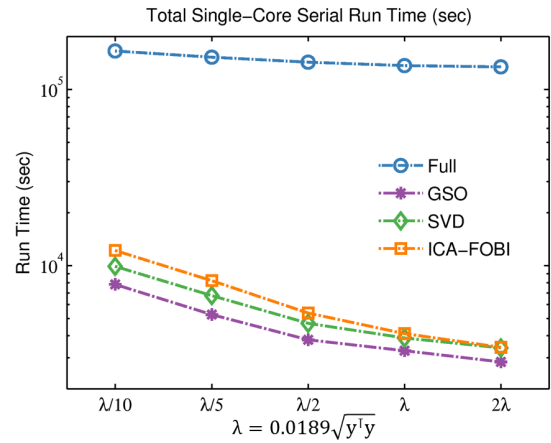


Fig. 11. Matched total single-core serial run time to reconstruct ADMIRE B-mode images shown in Fig. 7(a). The run times were measured and plotted as a function of λ that controls the degrees of freedom used when implementing ADMIRE.

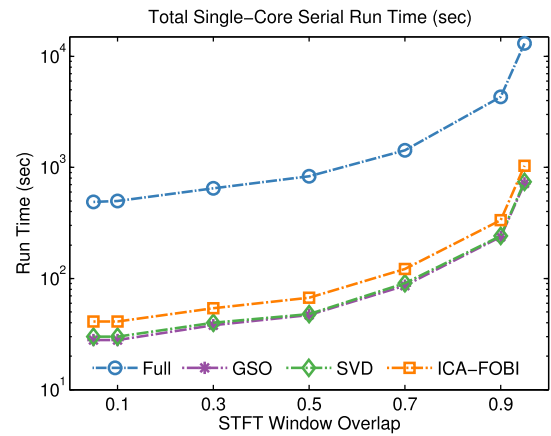


Fig. 12. Matched total single-core serial run time to form the ADMIRE images demonstrated in Fig. 10. The run times are a function of STFT window overlap ratio.

qualitative degradation is not noticeable. Using the measured CNR values demonstrated in Fig. 10(b), we conducted a Mann Whitney test (i.e., a Wilcoxon rank sum test) for $p < 0.05$, showing the differences were not significant for any cases when compared between 5% and 90% STFT window overlap. This result further supports reducing the overlap ratio of 90% used for the original ADMIRE implementation.

F. Timing Assessment

Table VI summarizes the results of measuring total single-core serial run-times from the matched data in Fig. 8. It is not surprising that an ICA-FOBI model requires a slightly longer run-time than the other two reduced models because of the greater number of nonzero coefficients. However, because ADMIRE using an ICA-FOBI model can reduce the run-time and preserve a similar performance to ADMIRE using a full model, the usefulness and benefits of an ICA-FOBI reduced model are substantial.

Fig. 11 shows the timing results using various λ values when applied to *in vivo* liver data, indicating that smaller values of

TABLE VI
TOTAL SINGLE-CORE SERIAL RUN TIME (SEC)

	Full Model	GSO Model	SVD Model	ICA-FOBI Model
Simulated phantom	4,308	237	242	336
<i>in vivo</i> liver scan	136,760	3,294	3,888	4,110

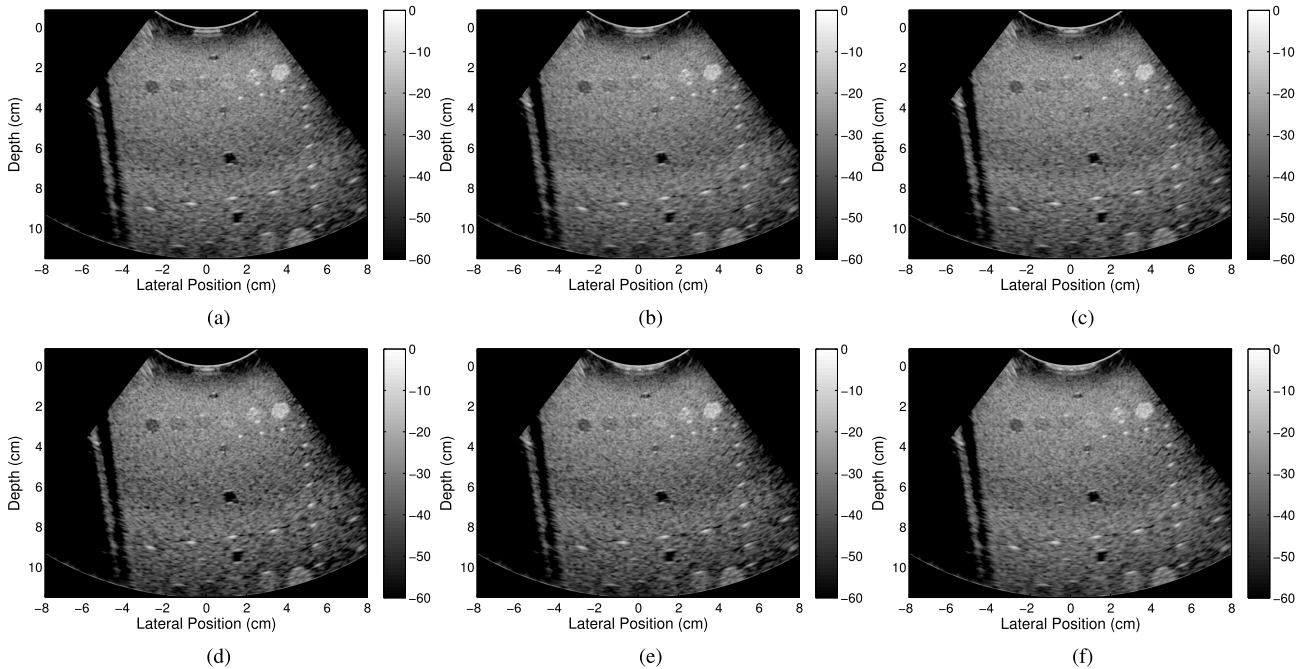


Fig. 13. Five ICA algorithms comparison using tissue-mimicking phantom images formed after using a full model and an ICA-based reduced model, along with the ADMIRE resulting image using (a) a full model. (b)–(f) images are post-ADMIRE images using an ICA-based reduced model with five different ICA algorithms, including (b) FOBI, (c) robustICA, (d) EBM, (e) SOBI, and (f) AMUSE. The dynamic range is 60 dB.

λ (i.e., higher degrees of freedom) require a longer run time when implementing ADMIRE, compared to cases of using higher λ values (i.e., lower degrees of freedom). As expected, ADMIRE may have a higher computational cost when implemented in higher clutter environments using higher degrees of freedom.

We also measured the corresponding total single-core run-time as a function of STFT window overlap in Fig. 12. It is important to note that the use of a 50% STFT window overlap can accelerate ADMIRE’s serial run time by more than one order of magnitude, when compared to the use of a 90% STFT window overlap, despite no substantial difference between images, as shown in Fig. 10.

G. Comparison of Models Reduced Using Different ICA Algorithms

Fig. 13 demonstrates the qualitative comparison results, including tissue-mimicking phantom B-mode images resulting from ADMIRE using: 1) a full model, a set of ICA-based reduced models using an algorithm called; 2) FOBI; 3) robustICA; 4) EBM; 5) SOBI; and 6) AMUSE. We then quantified the matched contrast, CNR, and SSNR to identify which ICA algorithm is superior in terms of producing a high-quality ADMIRE image. Table VII reports the quantitative results.

TABLE VII
QUANTITATIVE RESULTS USING DIFFERENT ICA ALGORITHMS

	Contrast (dB)	CNR (dB)	SSNR
DAS	8.78	1.10	2.03
Full	11.47	1.24	2.02
ICA-FOBI	11.66	1.40	2.12
ICA-robustICA	11.55	1.32	2.08
ICA-EBM	12.66	0.80	1.87
ICA-SOBI	12.41	0.85	1.88
ICA-AMUSE	11.70	1.12	1.93

Note that the ICA-FOBI and robust ICA algorithms show better performance than the others. The EBM and SOBI methods boost perceived contrast but decrease CNR and SSNR with degraded speckle texture. These methods may produce the limitations we found in ADMIRE using a GSO-based and an SVD-based reduced model.

IV. DISCUSSION AND CONCLUSION

We conducted a comprehensive analysis of the dimensionality reduced model methods to identify the usefulness

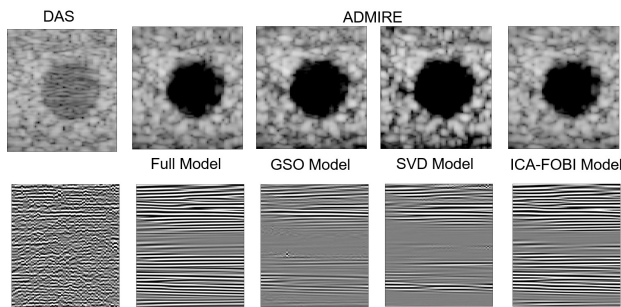


Fig. 14. Set of simulated cyst B-mode and the matched reconstructed channel data images using the four different ADMIRE models (full, GSO, SVD, and ICA-FOBI), along with DAS.

when implementing ADMIRE. A model reduced using an ICA-FOBI method is the most efficient way to accelerate ADMIRE implementation while preserving ADMIRE performance. The simulation, experimental phantom, and *in vivo* results demonstrated in Figs. 4, 6, and 7 indicate that an ICA-FOBI model may enable ADMIRE to perform as well as in the case of using a full model. The model predictors are nonstationary sinusoids that have substantial higher order correlations. We aim to minimize the correlations using the dimensionality reduction methods. The ICA method removes higher order correlations with a set of transformed model predictors with statistically independent vectors, while two other reduction methods (i.e., GSO and SVD) use orthonormal column vectors that are linearly independent and remove up to the second-order dependencies [34]. Fig. 14 shows a set of simulated cyst B-mode and the matched reconstructed channel data images using the four different ADMIRE models (full, GSO, SVD, and ICA-FOBI), along with DAS. Also, note that the number of predictors of the ICA-FOBI model is reduced by apparently three orders of magnitude.

It is also worth noting that reducing STFT window overlap (default setting in ADMIRE implementation is 90%) may remarkably increase algorithmic efficiency and decrease computational complexity. Based on the findings demonstrated in Figs. 10 and 12, a 50% STFT window overlap does not result in any significant loss of image quality while speeding up ADMIRE implementation by over one order of magnitude. A combination of using a reduced model method with different levels of STFT window overlap makes ADMIRE more computationally efficient.

The goal of this study was to reduce the ADMIRE algorithm's computational complexity without sacrificing the performance. However, more work needs to be done to further accelerate ADMIRE toward a real-time implementation. Given the state-of-the-art machine learning techniques, model decomposition (i.e., model-fit) using elastic-net regularization could be improved by replacing it with a support vector machine (SVM) with graphics processing unit (GPU) support [62]. Recently, the deep neural networks (DNNs) have been applied for ultrasound beamforming [36]. These findings from recent studies in machine learning suggest the robustness of neural networks and deep learning algorithms which could imitate the ADMIRE algorithm, enabling the

direct computation of post-ADMIRE decluttered signals from the input of cluttered channel data. It may also be possible to create an end-to-end deep network where cluttered channel data in the time domain are converted to ADMIRE decluttered channel data at the output. New architectures such as U-Net [63], generative adversarial networks (GANs) [64], or cyclical GANs [65] may be useful for this approach.

ACKNOWLEDGMENT

The authors would like to thank the staff of the Vanderbilt University ACCRE Computing Resource.

REFERENCES

- [1] T. L. Szabo, *Diagnostic Ultrasound Imaging: Inside Out*. New York, NY, USA: Academic, 2004.
- [2] W. M. Marks, *Ultrasound: A Practical Approach*. CreateSpace North Carolina, 2012.
- [3] K. D. Lindor et al., "The role of ultrasonography and automatic-needle biopsy in outpatient percutaneous liver biopsy," *Hepatology*, vol. 23, no. 5, pp. 1079–1083, 1996.
- [4] M. Ahmed et al., "Image-guided tumor ablation: Standardization of terminology and reporting criteria—A 10-year update," *Radiology*, vol. 273, no. 1, pp. 241–260, 2014.
- [5] M. Baad, Z. F. Lu, I. Reiser, and D. Paushter, "Clinical significance of US artifacts," *RadioGraphics*, vol. 37, no. 5, pp. 1408–1423, 2017.
- [6] J. T. Bushberg and J. M. Boone, *The Essential Physics of Medical Imaging*. Philadelphia, PA, USA: Lippincott Williams & Wilkins, 2011.
- [7] R. S. C. Cobbold, *Foundations of Biomedical Ultrasound*. London, U.K.: Oxford Univ. Press, 2007.
- [8] S. W. Flax and M. O'Donnell, "Phase-aberration correction using signals from point reflectors and diffuse scatterers: Basic principles," *IEEE Trans. Ultrason., Ferroelectr., Freq. Control*, vol. UFFC-35, no. 6, pp. 758–767, Nov. 1988.
- [9] M. O'Donnell and S. W. Flax, "Phase aberration measurements in medical ultrasound: Human studies," *Ultrason. Imag.*, vol. 10, no. 1, pp. 1–11, 1988.
- [10] M. Anderson, M. McKeag, and G. Trahey, "The impact of sound speed errors on medical ultrasound imaging," *J. Acoust. Soc. Amer.*, vol. 107, no. 6, pp. 3540–3548, 2000.
- [11] P. C. Tay, S. T. Acton, and J. A. Hossack, "A wavelet thresholding method to reduce ultrasound artifacts," *Computerized Med. Imag. Graph.*, vol. 35, no. 1, pp. 42–50, 2011.
- [12] G. F. Pinton, G. E. Trahey, and J. J. Dahl, "Sources of image degradation in fundamental and harmonic ultrasound imaging using nonlinear, full-wave simulations," *IEEE Trans. Ultrason., Ferroelectr., Freq. Control*, vol. 58, no. 6, pp. 754–765, Apr. 2011.
- [13] J. J. Dahl and N. M. Sheth, "Reverberation clutter from subcutaneous tissue layers: Simulation and *in vivo* demonstrations," *Ultrasound Med. Biol.*, vol. 40, no. 4, pp. 714–726, 2014.
- [14] B. Byram and M. Jakovljevic, "Ultrasonic multipath and beamforming clutter reduction: A chirp model approach," *IEEE Trans. Ultrason., Ferroelectr., Freq. Control*, vol. 61, no. 3, pp. 428–440, Mar. 2014.
- [15] M. Fink, "Time reversal of ultrasonic fields. I. Basic principles," *IEEE Trans. Ultrason., Ferroelectr., Freq. Control*, vol. 39, no. 5, pp. 555–566, Sep. 1992.
- [16] T. Christopher, "Finite amplitude distortion-based inhomogeneous pulse echo ultrasonic imaging," *IEEE Trans. Ultrason., Ferroelectr., Freq. Control*, vol. 44, no. 1, pp. 125–139, Jan. 1997.
- [17] P.-C. Li and M.-L. Li, "Adaptive imaging using the generalized coherence factor," *IEEE Trans. Ultrason., Ferroelectr., Freq. Control*, vol. 50, no. 2, pp. 128–141, Feb. 2003.
- [18] Q. Ma, Y. Ma, X. Gong, and D. Zhang, "Improvement of tissue harmonic imaging using the pulse-inversion technique," *Ultrasound Med. Biol.*, vol. 31, no. 7, pp. 889–894, 2005.
- [19] I. K. Holfort, F. Gran, and J. A. Jensen, "Broadband minimum variance beamforming for ultrasound imaging," *IEEE Trans. Ultrason., Ferroelectr., Freq. Control*, vol. 56, no. 2, pp. 314–325, Feb. 2009.

- [20] S. P. Näsholm, R. Hansen, S.-E. Måsøy, T. F. Johansen, and B. A. Angelsen, "Transmit beams adapted to reverberation noise suppression using dual-frequency surf imaging," *IEEE Trans. Ultrason., Ferroelectr., Freq. Control*, vol. 56, no. 10, pp. 2124–2133, Oct. 2009.
- [21] M. A. Ellis, F. Viola, and W. F. Walker, "Super-resolution image reconstruction using diffuse source models," *Ultrasound Med. Biol.*, vol. 36, no. 6, pp. 967–977, 2010.
- [22] M. A. Lediju, G. E. Trahey, B. C. Byram, and J. J. Dahl, "Short-lag spatial coherence of backscattered echoes: Imaging characteristics," *IEEE Trans. Ultrason., Ferroelectr., Freq. Control*, vol. 58, no. 7, pp. 1377–1388, Jul. 2011.
- [23] B. Byram, K. Dei, J. Tierney, and D. Dumont, "A model and regularization scheme for ultrasonic beamforming clutter reduction," *IEEE Trans. Ultrason., Ferroelectr., Freq. Control*, vol. 62, no. 11, pp. 1913–1927, Nov. 2015.
- [24] Y. Yankelevsky, Z. Friedman, and A. Feuer, "Component-based modeling and processing of medical ultrasound signals," *IEEE Trans. Signal Process.*, vol. 65, no. 21, pp. 5743–5755, Nov. 2017.
- [25] M. Jakovljevic, S. Hsieh, R. Ali, G. C. L. Kung, D. Hyun, and J. J. Dahl, "Local speed of sound estimation in tissue using pulse-echo ultrasound: Model-based approach," *J. Acoust. Soc. Amer.*, vol. 144, no. 1, pp. 254–266, 2018.
- [26] A. Bradley, J. Yao, J. Dewald, and C.-P. Richter, "Evaluation of electroencephalography source localization algorithms with multiple cortical sources," *PLoS ONE*, vol. 11, no. 1, 2016, Art. no. e0147266.
- [27] C. Dinh, D. Strohmeier, M. Luessi, D. Güllmar, D. Baumgarten, J. Haueisen, and M. S. Hämäläinen, "Real-time MEG source localization using regional clustering," *Brain Topogr.*, vol. 28, no. 6, pp. 771–784, 2015.
- [28] K. Dei and B. C. Byram, "The impact of model-based clutter suppression on cluttered, aberrated wavefronts," *IEEE Trans. Ultrason., Ferroelectr., Freq. Control*, vol. 64, no. 10, pp. 1450–1464, Oct. 2017.
- [29] K. Dei and B. Byram, "A robust method for ultrasound beamforming in the presence of off-axis clutter and sound speed variation," *Ultrasonics*, vol. 89, pp. 34–45, Sep. 2018.
- [30] K. Dei, J. E. Tierney, and B. C. Byram, "Model-based beamforming with plane wave synthesis in medical ultrasound," *Proc. SPIE*, vol. 5, no. 2, 2018, Art. no. 027001.
- [31] K. Dei and B. Byram, "Computationally-efficient model-based clutter suppression with ADMIRE," in *Proc. IEEE Int. Ultrason. Symp. (IUS)*, Sep. 2016, pp. 1–4.
- [32] G. B. Arfken and H.-J. Weber, *Mathematical Methods for Physicists*. New York, NY, USA: Academic, 1970.
- [33] S. S. Bayin, *Essentials of Mathematical Methods in Science and Engineering*. Hoboken, NJ, USA: Wiley, 2013.
- [34] A. Hyvärinen, J. Karhunen, and E. Oja, *Independent Component Analysis*. Hoboken, NJ, USA: Wiley, 2001.
- [35] J. Shin and L. Huang, "Spatial prediction filtering of acoustic clutter and random noise in medical ultrasound imaging," *IEEE Trans. Med. Imag.*, vol. 36, no. 2, pp. 396–406, Feb. 2017.
- [36] A. C. Luchies and B. C. Byram, "Deep neural networks for ultrasound beamforming," *IEEE Trans. Med. Imag.*, vol. 37, no. 9, pp. 2010–2021, Sep. 2018.
- [37] H. Zou and T. Hastie, "Regularization and variable selection via the elastic net," *J. Roy. Statist. Soc., B (Statistical Methodology)*, vol. 67, no. 2, pp. 301–320, 2005.
- [38] B. Yang, "A study of inverse short-time Fourier transform," in *Proc. IEEE Int. Conf. Acoust., Speech Signal Process.*, Mar./Apr. 2008, pp. 3541–3544.
- [39] R. J. Tibshirani and J. Taylor, "Degrees of freedom in lasso problems," *Ann. Statist.*, vol. 40, no. 2, pp. 1198–1232, 2012.
- [40] J. Nash, "The singular-value decomposition and its use to solve least-squares problems," in *Compact Numerical Methods for Computers: Linear Algebra and Function Minimisation*. New York, NY, USA: Routledge, 1990, pp. 30–48.
- [41] X. Liu, Z. Wen, and Y. Zhang, "Limited memory block Krylov subspace optimization for computing dominant singular value decompositions," *SIAM J. Sci. Comput.*, vol. 35, no. 3, pp. A1641–A1668, 2013.
- [42] A. Hyvärinen and E. Oja, "Independent component analysis: Algorithms and applications," *Neural Netw.*, vol. 13, nos. 4–5, pp. 411–430, 2000.
- [43] J. Wang and C.-I. Chang, "Independent component analysis-based dimensionality reduction with applications in hyperspectral image analysis," *IEEE Trans. Geosci. Remote Sens.*, vol. 44, no. 6, pp. 1586–1600, Jun. 2006.
- [44] J. Shlens, "A tutorial on independent component analysis," 2014, *arXiv:1404.2986*. [Online]. Available: <https://arxiv.org/abs/1404.2986>
- [45] T. Adali, H. Li, M. Novey, and J. Cardoso, "Complex ICA using nonlinear functions," *IEEE Trans. Signal Process.*, vol. 56, no. 9, pp. 4536–4544, Sep. 2008.
- [46] J.-F. Cardoso, "Source separation using higher order moments," in *Proc. Int. Conf. Acoust., Speech, Signal Process. (ICASSP)*, 1989, pp. 2109–2112.
- [47] A. Hyvärinen, "Fast and robust fixed-point algorithms for independent component analysis," *IEEE Trans. Neural Netw.*, vol. 10, no. 3, pp. 626–634, May 1999.
- [48] V. Zarzoso and P. Comon, "Robust independent component analysis by iterative maximization of the kurtosis contrast with algebraic optimal step size," *IEEE Trans. Neural Netw.*, vol. 21, no. 2, pp. 248–261, Feb. 2010.
- [49] *RobustICA Algorithm for Independent Component Analysis*. Accessed: Apr. 1, 2018. [Online]. Available: <http://www.i3s.unice.fr/~zarzoso/robustica.html>
- [50] X.-L. Li and T. Adali, "Independent component analysis by entropy bound minimization," *IEEE Trans. Signal Process.*, vol. 58, no. 10, pp. 5151–5164, Oct. 2010.
- [51] X.-L. Li and Tulay Adali, "Complex independent component analysis by entropy bound minimization," *IEEE Trans. Circuits Syst. I, Reg. Papers*, vol. 57, no. 7, pp. 1417–1430, Jul. 2010.
- [52] *Independent Component Analysis (ICA) by Entropy Bound Minimization (EBM) and Entropy Rate Minimization (ERM)*. Accessed: Apr. 1, 2018. [Online]. Available: http://www.mlsp.umbc.edu/ica_ebm.html
- [53] A. Belouchrani, K. Abed-Meraim, J.-F. Cardoso, and E. Moulines, "A blind source separation technique using second-order statistics," *IEEE Trans. Signal Process.*, vol. 45, no. 2, pp. 434–444, Feb. 1997.
- [54] L. Tong, R. Liu, V. C. Soon, and Y.-F. Huang, "Indeterminacy and identifiability of blind identification," *IEEE Trans. Circuits Syst.*, vol. 38, no. 5, pp. 499–509, May 1991.
- [55] J. A. Jensen and N. B. Svendsen, "Calculation of pressure fields from arbitrarily shaped, apodized, and excited ultrasound transducers," *IEEE Trans. Ultrason., Ferroelectr., Freq. Control*, vol. 39, no. 2, pp. 262–267, Mar. 1992.
- [56] J. A. Jensen, "FIELD: A program for simulating ultrasound systems," in *Proc. 10th Nordic-Baltic Conf. Biomed. Imag.*, vol. 4, pp. 351–353, Jan. 1996.
- [57] R. F. Wagner, S. W. Smith, J. M. Sandrik, and H. Lopez, "Statistics of speckle in ultrasound B-scans," *IEEE Trans. Sonics Ultrason.*, vol. SU-30, no. 3, pp. 156–163, May 1983.
- [58] B. Byram and J. Shu, "Pseudononlinear ultrasound simulation approach for reverberation clutter," *Proc. SPIE*, vol. 3, no. 4, 2016, Art. no. 46005.
- [59] B. Byram and J. Shu, "A pseudo non-linear method for fast simulations of ultrasonic reverberation," *Proc. SPIE*, vol. 9790, Apr. 2016, Art. no. 97900U.
- [60] O. M. H. Rindal, A. Rodriguez-Molares, and A. Austeng, "The dark region artifact in adaptive ultrasound beamforming," in *Proc. IEEE Int. Ultrason. Symp. (IUS)*, Sep. 2017, pp. 1–4.
- [61] K. Dei, A. Luchies, and B. Byram, "Contrast ratio dynamic range: A new beamformer performance metric," in *Proc. IEEE Int. Ultrason. Symp. (IUS)*, Sep. 2017, pp. 1–4.
- [62] Q. Zhou, W. Chen, S. Song, J. R. Gardner, K. Q. Weinberger, and Y. Chen, "A reduction of the elastic net to support vector machines with an application to GPU computing," in *Proc. AAAI*, 2015, pp. 3210–3216.
- [63] O. Ronneberger, P. Fischer, and T. Brox, "U-Net: Convolutional networks for biomedical image segmentation," in *Proc. Int. Conf. Med. Image Comput. Comput.-Assist. Intervent. Cham, Switzerland: Springer*, 2015, pp. 234–241.
- [64] P. Isola, J.-Y. Zhu, T. Zhou, and A. A. Efros, "Image-to-image translation with conditional adversarial networks," in *Proc. IEEE Conf. Comput. Vis. Pattern Recognit.*, Jul. 2017, pp. 1125–1134.
- [65] J.-Y. Zhu, T. Park, P. Isola, and A. A. Efros, "Unpaired image-to-image translation using cycle-consistent adversarial networks," in *Proc. IEEE Int. Conf. Comput. Vis.*, Oct. 2017, pp. 2223–2232.



Kazuyuki Dei was born in Saitama, Japan. He received the B.S. degree in mechanical engineering from the University of California at Berkeley, Berkeley, CA, USA, in 2000, and the Ph.D. degree in biomedical engineering from Vanderbilt University, Nashville, TN, USA, in 2019.

He was with Fujitsu Ltd., Tokyo, Japan, and with Fujitsu Semiconductor America Inc., Sunnyvale, CA, USA, as an Electrical Design and Development Engineer. His research interests include model-based acoustic clutter suppression, phase-aberration mea-

surements, beamforming, and signal and image processing.



Siegfried Schlunk (S'17) was born in Nashville, TN, USA. He received the B.E. degree in biomedical engineering and mathematics from Vanderbilt University, Nashville, TN, USA, in 2016. He is currently pursuing the Ph.D. degree in biomedical engineering with Vanderbilt University.

His research interests focus on developing methods for improving ultrasound image quality in cardiac and kidney applications.



Brett Byram (M'15) received the B.S. degree in biomedical engineering and math from Vanderbilt University, Nashville, TN, USA, in 2004, and the Ph.D. degree in biomedical engineering from Duke University, Durham, NC, USA.

He was a Research Assistant Professor with Duke University. In 2013, he joined the Biomedical Engineering Department at Vanderbilt University, Nashville, TN, USA, as an Assistant Professor. He has spent time working in the Jørgen Jensen's Center for Fast Ultrasound, Lyngby, Denmark, and also in

Siemens Healthcare's ultrasound division, Mountain View, CA, USA. He currently runs the Biomedical Elasticity and Acoustic Measurement (BEAM) Laboratory, where he and others in the lab pursue solutions to clinical problems using ultrasound. He is also with the Vanderbilt Institute for Surgery and Engineering (VISE) and the Vanderbilt University Institute of Imaging Science (VUIIS). His research interests include beamforming, motion estimation, and other related signal processing and hardware development tasks.